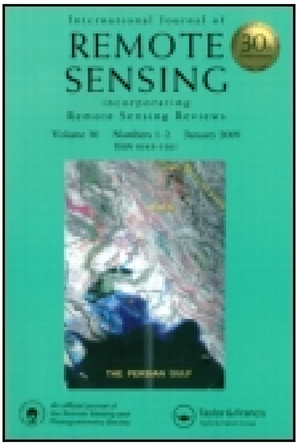

International Journal of Remote Sensing
Publication details, including instructions for authors and subscription information:
http://www.tandfonline.com/loi/tres20

Earth science applications of ICESat/GLAS: a review

Xianwei Wang [a], Xiao Cheng [b], Peng Gong [a c], Huabing Huang [a], Zhan Li [a] & Xiaowen Li [a]

[a] State Key Laboratory of Remote Sensing Science, Jointly Sponsored by Institute of Remote Sensing Applications, Chinese Academy of Sciences and Beijing Normal University, Da Tun Road, Beijing, 100101, China

[b] College of Global Change and Earth System Science, Beijing Normal University, Xin Jie Kou Wai Street, Beijing, 100860, China

[c] Center for Earth System Science, Tsinghua University, Beijing, 100084, China

Available online: 11 Aug 2011

To cite this article: Xianwei Wang, Xiao Cheng, Peng Gong, Huabing Huang, Zhan Li & Xiaowen Li (2011): Earth science applications of ICESat/GLAS: a review, International Journal of Remote Sensing, 32:23, 8837-8864

To link to this article: http://dx.doi.org/10.1080/01431161.2010.547533

International Journal of Remote Sensing
Vol. 32, No. 23, 10 December 2011, 8837–8864

Taylor & Francis
Taylor & Francis Group

Review Article

Earth science applications of ICESat/GLAS

XIANWEI WANG†, XIAO CHENG‡, PENG GONG*†§, HUABING HUANG†, ZHAN LI† and XIAOWEN LI†

†State Key Laboratory of Remote Sensing Science, Jointly Sponsored by Institute of Remote Sensing Applications, Chinese Academy of Sciences and Beijing Normal University, Da Tun Road, Beijing 100101, China

‡College of Global Change and Earth System Science, Beijing Normal University, Xin Jie Kou Wai Street, Beijing 100860, China

§Center for Earth System Science, Tsinghua University, Beijing 100084, China

(*Received 7 October 2010; in final form 26 November 2010*)

The Ice, Cloud, and Land Elevation Satellite (ICESat) completed 19 successful campaigns for Earth observation missions following its launch in 2003. The Geoscience Laser Altimeter System (GLAS) on board ICESat provided data of high quality with unprecedented accuracy over the globe. The three laser sensors of GLAS acquired a large volume of data between 2003 and 2009. These data were used widely to detect changes in Greenland and Antarctic ice sheets and to determine forest heights, sea-ice freeboard heights and the distribution of cloud and aerosols. Here, we provide a review of these applications, describe the methodology involved in GLAS data processing and summarize some of the challenges to make better use of GLAS data. Other applications, including ice-sheet slope extraction, distinguishing between water, bare land, urban building and high forest, urban building height extraction, changes in glaciers and ice caps and water levels in lakes are discussed more briefly.

1. Introduction

Variation in surface elevation at the global scale is an important factor in global environmental change. A number of satellite sensors have been developed to obtain Earth-surface elevation data. Radar altimeters, such as those on board Seasat and Geosat, were first developed with a primary goal of studying the ocean surface, in particular, determining the geoid (Cooper and Hinton 1996; Berry 2000). Information on significant wave height and near sea-surface wind speed can also be derived from the radar returns (Tokmakian *et al*. 1994). Currently, radar altimeter data are obtained mainly from Jason-1, ERS-1/2 (European Remote Sensing Satellite), TOPEX (Ocean Topography Experiment) and ENVISAT (Environmental Satellite) (e.g. Papa *et al*. 2003, Legresy *et al*. 2005, Chambers 2007, Klokočník *et al*. 2008). The characteristics of the altimeters on board these satellites are listed in table 1. The successful application potential of altimetry data in other aspects apart from oceanography has also been demonstrated, including mapping polar ice sheets, monitoring sea-ice margins (McIntyre 1991, Cudlip and Milnes 1994) and studying sea ice, land surfaces and ice

*Corresponding author. Email: gong@irsa.ac.cn

International Journal of Remote Sensing
ISSN 0143-1161 print/ISSN 1366-5901 online
http://www.tandf.co.uk/journals
http://dx.doi.org/10.1080/01431161.2010.547533

Table 1. Characteristics of different satellite-borne microwave altimeters and ICESat.

	ERS-1/2(RA)	ENVISAT (RA-2)	TOPEX/ Poseidon	Jason-1/ Poseidon2	ICESat
Orbit altitude (km)	785	785	1336	1336	600
Inclination (°)	98.52	98.55	66	66	94
Footprint (km)*	~7	2–10	~5	~5	0.075
Pulse transmitted	13.8 GHz	13.575 GHz 3.2 GHz	13.6 GHz 5.3 GHz	13.6 GHz 5.3 GHz	1064 nm 532 nm
Mission duration (year)	1991–2003	2002–2008	1992–2006	2001–	2003–2009

Note: *Diameter of altimeter footprint over land.

caps (Fabrice *et al*. 2003, Benoit *et al*. 2005, Laurence *et al*. 2009), as well as detecting water-level changes in wetlands (Kim *et al*. 2009). However, the accuracy of radar altimetry in the determination of land-surface elevation is limited by its large footprint, which has a diameter of several kilometres, see table 1. Over sloping areas, the slope-induced error varies from several metres to tens of metres. The microwaves used in altimetry belong to the K_u band, and this has the consequence that snow-surface elevation cannot be determined accurately because K_u band microwaves can penetrate through snow to the snow/ice interface (Connor *et al*. 2009). The large footprints of radar altimeters (table 1) can satisfy lower resolution mapping demands (several kilometres) with moderate height accuracy. For finer spatial resolution work, a better solution is to use a laser altimeter because of its smaller footprint and greater height accuracy.

ICESat was an experimental scientific satellite launched by the National Aeronautics and Space Administration (NASA) in January 2003 with the Geoscience Laser Altimeter System (GLAS), which comprises three lasers (Laser 1, Laser 2 and Laser 3) as the primary instruments on board. The primary purpose of the GLAS instrument is to detect ice-elevation changes in Antarctica and Greenland (Bae and Schutz 2002, Zwally *et al.* 2002). However, the application of these data reached far more aspects than the initial purpose. These data have been used widely in other fields, including deriving sea-ice freeboard, forest canopy height, cloud heights, aerosol-height distribution and land-terrain changes (Zwally 2010).

2. Characteristics of the ICESat/GLAS instrument

ICESat operates at a height of about 600 km with an inclination angle of 94°. Because of the small laser footprint, in order to obtain a dense ground-track coverage over the globe, a 183-day repeat cycle orbit was initially designed. However, two reference orbits have actually been used in operation: an 8-day repeat orbit and a 91-day repeat (with a 33 day subcycle) orbit. The 8-day interval was adopted to enable frequent repeats of the ground calibration sites during the lifetime of Laser 1, and the 91-day orbit was adopted to provide dense data for scientific usage (Schutz *et al*. 2005) for Laser 2 and Laser 3. In each campaign of Laser 2 or Laser 3, the laser keeps working for about 33 days, almost two or three times a year. At the global scale, GLAS provided full coverage of relatively fine-resolution satellite altimetry data from 2003 to 2009.

In addition to the three lasers, the scientific equipment onboard ICESat includes a global positioning system (GPS) and a star tracker (ST) (e.g. Schutz 1998, Zwally *et al*. 2002, Abshire *et al*. 2005, Schutz *et al*. 2005). The principle of height measurement (see figure 1) is as follows: the laser pulse transmitted from GLAS reaches the ground after interacting with clouds or aerosols in the atmosphere and is reflected back to the atmosphere, interacting with clouds and/or aerosols again. Finally, the laser pulse is received by the 1 m diameter telescope. The distance from the laser transmitter to the ground surface can be computed using:

$$d = ct/2, \tag{1}$$

where c is the speed of light and t is the flight time of the laser beam, which can be determined from the laser pulse transmitting time and receiving time.

During this process, the space location of GLAS can be determined by the GPS, and the orientation of the satellite can be obtained by the ST so that the location of the footprint on the ground can be determined. Based on these data, the ground elevation value and location are computed (see figure 1). However, this is just a coarse result, some corrections need to be done to rectify the range and location of each footprint, see, for example, Schutz (2002) and Sirota *et al*. (2005). The accuracy and precision of ICESat altimetry data are about 14 cm and 2 cm, respectively (Shuman *et al*. 2006). The error sources are listed in table 2.

The direction of GLAS is almost pointing to nadir (with a 0.3° bias), and the laser footprints on the ground are about 70 m in diameter spaced at about 172 m along the subsatellite track. The working frequency of GLAS is 40 Hz and two laser pulses with wavelengths of 532 and 1064 nm are transmitted (e.g. Zwally *et al*. 2002, Schutz *et al*. 2005). GLAS was the first polar-orbiting spaceborne laser altimeter system, and the horizontal precision of the ground footprints is about 6 m (Abshire *et al*. 2005). The GLAS footprints obviously become denser at higher latitude because the orbits get closer together, especially in the polar regions. The coverage of ICESat/GLAS extends to 86° S/N (to be compared with 81.5° S/N for ERS1/2) in latitude because of its 94° orbit inclination.

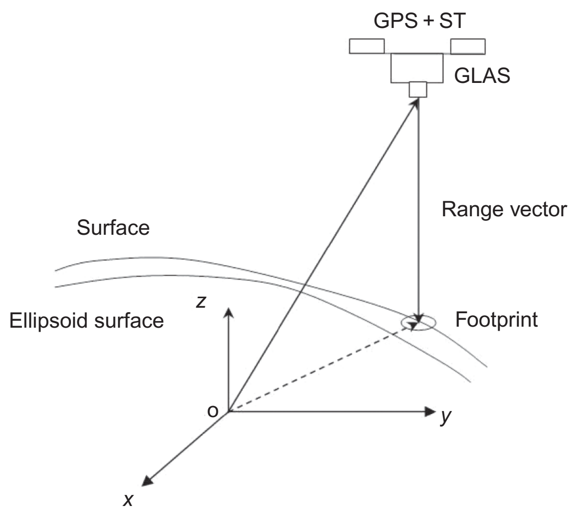

Figure 1. Altimetry concept of GLAS. They are the other two important instruments onboard ICESat. Oxyz is the defined geographic coordinate system.

Table 2. Single-shot error budget for ICESat elevation measurement (Zwally *et al*. 2002).

GLAS range measurement precision (cm)	10
Radial orbit determination (cm)	5
Pointing determination (cm)	7.5
Atmospheric delay (cm)	2
Atmospheric forward scattering (cm)	2
Other (cm)	1
Residual sum of square (RSS) (cm)	13.8

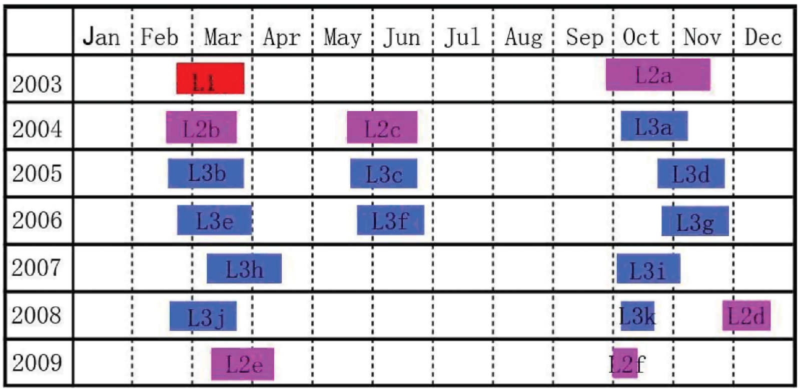

Figure 2. Missions of ICESat/GLAS. Different colours stand for different lasers: red, Laser 1; pink, Laser 2; blue, Laser 3; and the lengths of the bars show the durations of different missions. There are a total of 18 colour bars and L1a (20 February 2003 to 21 March 2003) and L1b (21 March 2003 to 29 March 2003) are shown as one bar L1.

ICESat/GLAS successfully carried out 19 campaigns until the mission was terminated. In order to maintain a 3–5 year life span, the three laser transmitters were operated individually. For each campaign, there is an identifier, such as L2b to denote Laser 2 and operation period b, see figure 2. However, the instruments did not operate exactly as expected. On 29 March 2003, Laser 1 stopped working (Kichak 2003, Abshire *et al*. 2005) and on 21 May 2005, Laser 2 stopped working because of its rapid energy loss caused by photodarkening at or near the laser's frequency doubler (Allan 2008, Abdalati *et al*. 2010). Laser 3 stopped working after 14 days in campaign L3k in October 2008. After that, Laser 2 was restarted again and expired on 11 October 2009.

Based on the waveform of the received laser pulse and other instrument records, 15 different kinds of data (e.g. Zwally *et al*. 2002, Schutz *et al*. 2005), described as GLA01, GLA02, . . . , GLA15, are derived after processing. These data can be separated into three levels as L1A, L1B and L2, and the most advanced data level is L2, including cloud and aerosol data, planetary boundary data, sea-ice and sea-elevation data, ice-sheet-elevation data and land-elevation data (see table 3). These different levels of data have been widely used in oceanographic and sea-ice thickness studies, cloud-height determination and vertical distribution of aerosols in the atmosphere, land-elevation changes, biomass information extraction and polar ice-sheet change detection. The structure of different kinds of data was given by Brittingham and Lee (2005).

Table 3. Description of GLAS data (NSIDC).

Data products	Data description
GLA01	L1A Global altimetry data
GLA02	L1A Global atmosphere data
GLA03	L1A Global engineering data
GLA04	L1A Global laser pointing data
GLA05	L1B Global waveform-based range corrections data
GLA06	L1B Global elevation data
GLA07	L1B Global backscatter data
GLA08	L2 Global planetary boundary layer and elevated aerosol layer height
GLA09	L2 Global cloud heights for multi-layer clouds
GLA10	L2 Global aerosol vertical structure data
GLA11	L2 Global thin-cloud/aerosol optical depths data
GLA12	L2 Antarctica and Greenland ice-sheet altimetry data
GLA13	L2 Sea-ice altimetry data
GLA14	L2 Global land-surface altimeter data
GLA15	L2 Ocean altimeter data

3. Major applications of GLAS data and discussion of methods

3.1 *Measurement of sea-ice freeboard and thickness*

Sea ice plays an important role in global climate-change studies, especially in polar regions (Laxon *et al*. 2003). Sea ice reflects the incident sunlight greatly and absorbs only a small amount of solar energy. If the extent of sea ice decreased or increased to a large extent, it would change the local energy budget and the global climate greatly (Cavalieri and Markus 2006). Recent studies show that Arctic sea ice is thinning (e.g. Rothrock *et al*. 1999, Lindsay and Zhang 2005). Traditionally, from remotely sensed images acquired by different satellites, the horizontal distribution of sea ice can be determined. However, it is difficult to obtain elevation information about sea ice with traditional imaging sensors. Satellite altimetry makes this possible. The first example of ice freeboard (the part of sea ice above the sea surface) measurement with a radar altimeter was described by Laxon *et al*. (2003). With earlier active microwave data, only lower resolution elevation data at the scale of several square kilometres can be derived. Over larger ground irradiation areas, the precision decreases due to the complexity of the return waveform after interacting with the ground (Brenner *et al*. 2007).

Sea-ice thickness (including the snow depth on the sea ice) extraction can be divided into two parts: first, sea-ice freeboard is derived, and then ice thickness is obtained by assuming hydrostatic equilibrium. Knowledge of sea-surface height is crucial to freeboard extraction. The freeboard H_{f} (see figure 3) can be calculated by subtracting the sea-surface height from the sea-ice height:

$$H_{\mathrm{f}} = H_{\mathrm{si}} - H_{\mathrm{ss}}, \tag{2}$$

where H_{f} is the freeboard (from the sea surface to the top of the sea ice plus its snow-cover depth), H_{si} is the sea-ice height and H_{ss} is the sea-surface height.

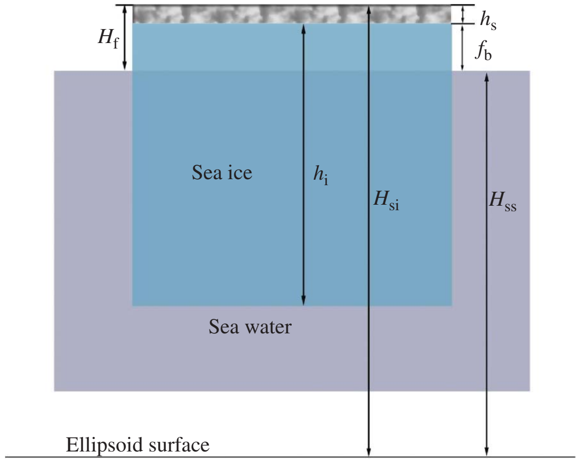

Figure 3. Sketch map of sea-ice thickness measurement.

Sea-surface height (H_{ss}) is the base to derive freeboard, which traditionally can be achieved by different models considering geoid undulation, tidal contribution, atmospheric pressure and dynamic topography associated with geostrophic surface currents. The discussion on sea surface and these four parts were detailed by Kwok *et al*. (2006). However, the modelled surface is not precise enough to determine the actual sea surface because not every part is well known.

Different methods for the determination of sea-surface elevation have been developed by many researchers. There are at least six methods to determine it.

1. Laxon *et al*. (2003) first gave an example of freeboard measurement from a radar altimeter with sea-surface height determined by open water or thin-ice measurements through the analysis of return echoes.
2. Kwok *et al*. (2004) gave a first look at Arctic sea-ice freeboard with the sea surface determined by new openings of the sea using a method that analyses near-coincident ICESat and RADARSAT imagery. However, snow depth is the greatest uncertainty in the conversion from freeboard to ice thickness.
3. Forsberg and Skourup (2005) combined Arctic Gravity Project data and Gravity Recovery and Climate Experiment data to derive a new geoid model and select the lowest values from geoid-subtracted ICESat data (ICESat tide-corrected data with ellipsoid height subtracting the geoid height) to represent the sea surface with a correlation length of 20 km along track. However, in some heavy ice conditions, the lowest values may correspond to thin ice, thus introducing a bias.
4. Kwok *et al*. (2006, 2007) proposed two alternative approaches to deriving sea-surface height. One involves detecting open water or newly frozen snow-free leads by comparing the reflectivity of the samples with that of the background ice and the expected deviation from the mean surface as the sea level. The other involves using a criterion that samples have an expected deviation from the mean surface as the sea-surface height. Because of a lower requirement, more

sea-surface points with a lower quality are selected than that of the previous method. However, these two methods tend to give a higher sea-surface level because sometimes the sea-surface level is contaminated by thin ice.

5. Zwally *et al*. (2008) developed an algorithm to extract sea surface with the lowest 2% of ICESat elevations in a 50 km segment. However, if 2% of the points correspond to thin ice rather than open water, there will be a bias in sea-surface determination.
6. Farrell *et al*. (2009) developed new criteria to derive sea-surface height in the Arctic by analysing a combination of ICESat parameters including surface elevation, reflectivity and the properties of the reflected laser waveform. This method is independent of synchronous image data and focuses on individual footprint analysis.

All the methods described above for sea-surface-height derivation are based on open water, leads and thin-ice area extraction. In practice, the method of combining near-coincident images with ICESat data may be problematic since near-coincident images do not always exist, but it gives best quality of leads detection to present sea-surface height. Other methods developed by Forsberg and Skourup (2005), Kwok *et al*. (2006, 2007), Zwally *et al*. (2008) and Farrell *et al*. (2009) can be used if local synchronous image data are not available. The thickness of thin ice is the primary uncertainty of these methods. In addition, less leads detected under different criteria than actual ones may not represent sea-surface level adequately. The determination of local sea-surface height is an area for further research because it is the base to directly derive freeboard and even sea-ice thickness.

Once the freeboard, H_f, is determined, it is straightforward to determine the thickness of the ice assuming hydrostatic equilibrium and a simple laminar geometrical shape of the sea ice:

$$h_i = \frac{\rho_s}{\rho_w - \rho_i} h_s + \frac{\rho_w}{\rho_w - \rho_i} f_b \tag{3}$$

and

$$h_s + f_b = H_f, \tag{4}$$

where ρ_s, ρ_i and ρ_w stand for snow, sea-ice and water densities, respectively (sometimes, they are given as constants (Zwally *et al*. 2008)), h_i is the thickness of sea ice, h_s is the thickness of the snow covering on the ice, f_b is the height from the sea surface to the snow-ice surface and H_f is the total freeboard from the water to the top of the sea ice plus the snow depth. H_f, f_b, h_s and h_i are depicted in figure 3. h_s can be calculated using Earth Observing System (EOS) Aqua Advanced Microwave Scanning Radiometer (AMSR-E) data (Cavalieri and Markus 2006, Zwally *et al*. 2008) or derived from available climate and meteorological data products (Kwok and Cunningham 2008). H_f can be derived from GLAS data by using equation (2). Thus, f_b can be derived using equation (4). Finally, h_i is calculated. When there is no snow covering on the sea ice or there is little snow, equations (3) and (4) simplify to:

$$h_i = \frac{\rho_w}{\rho_w - \rho_i} f_b \tag{5}$$

and

$$f_b = H_f. \tag{6}$$

Since the sea-ice thickness derivation is now primarily from freeboard conversion according to the buoyancy principle, further *in situ* measurement is necessary to validate the final results.

Many researchers have worked on the dynamic change of sea ice with ICESat/GLAS data. Kwok *et al*. (2004, 2006, 2007, 2008), Forsberg and Skourup (2005), Zwally *et al*. (2008) and Farrell *et al*. (2009) focused on sea-ice surface determination (described above), freeboard derivation and sea-ice thickness extraction. In addition, the results of freeboard derived from ICESat/GLAS data were compared with other results, such as airborne Light Detection and Ranging (LiDAR) data. Kurtz *et al*. (2008) determined the freeboard of sea ice north of Alaska from ICESat/GLAS data and compared it with that derived from a high-resolution airborne laser altimeter. The results showed a good agreement most of the time, but sometimes GLAS data underestimated the freeboard by up to 9 cm because occasionally thin ice is considered as the sea surface. Sea-ice dynamics and sea-ice characteristics, such as sea-ice roughness and sea-ice ridges, can also be obtained from GLAS data (Kwok *et al*. 2006). Farrell *et al*. (2009) used GLAS data from 2003 to 2008 to extract the 5-year freeboard changes of Arctic sea ice and found that the mean freeboard during the autumn and winter periods declined at a rate of about 1.8 cm yr^{-1} and 1.6 cm yr^{-1}, respectively.

3.2 *Change detection of Antarctic and Greenland ice-sheet elevation*

In polar areas, the primary precipitation is snowfall because of the low temperature. In the central polar areas, the accumulated snow packs into ice and gradually forms into ice sheets. The ice tends to flow under gravity to lower levels where some becomes glaciers and some becomes ice shelves (Rees 2006). In the austral summer, melting from ice shelves is an important source of water supply to the ocean. Therefore, the mass balance is a critical factor in global change and global warming. The influence of ice sheets on global change was discussed by Bamber *et al*. (2009), Clark *et al*. (1999) and Ivins (2009). According to the Intergovernmental Panel on Climate Change (IPCC 2007), sea level would increase by 5 m if the ice in western Antarctica melted completely. The sea level could rise by about 70 m if both the Greenland and Antarctic ice sheets melted completely (Alley *et al*. 2005). From 1992 to 1996, the changes of Antarctic ice-sheet elevation derived from altimeter data was determined to be an annual decrease of 0.9 ± 0.5 cm (Wingham *et al*. 1998). GLA12 data are produced for the purpose of studying changes in the Antarctic and Greenland ice sheets. Digital elevation models (DEMs) of Antarctica, with a resolution of approximately 500 m (Dimarzio *et al*. 2007a), and of Greenland, with a resolution of approximately 1000 m (Dimarzio *et al*. 2007b), which are critical to polar change research, can be freely obtained from the National Snow and Ice Data Center (NSIDC; http://nsidc.org/). ICESat/GLAS data can cover the whole of Greenland and most of the Antarctica ice sheet. There are at least three methods to obtain changes of ice-sheet elevation with GLAS data. These are summarized below.

1. Elevation change can be extracted by comparing ground overlapping footprints (Slobbe *et al*. 2008). Altimetry data from overlapping footprints from different campaigns can be extracted to derive changes. Since ICESat/GLAS adopts a near-polar and repeat orbit data collection strategy, ground overlapping footprints, which can be divided into repeat-track footprint pairs and cross-track footprint pairs (see figure 4), have been obtained during different campaigns. Repeat-track footprint pairs (see area B in figure 4) refer to laser footprints from repeat tracks that are in the same orientation. Cross-track footprint pairs (see area A in figure 4) refer to laser footprints from cross tracks that are in different orientations (one descending track and one ascending track). Therefore, this method is effective at higher latitudes where dense ground footprints are available. Adjacent footprints from different laser campaigns are selected for analysis if the distance between them is less than 70 m. If footprints are located in a flat area, comparisons between pairs that are farther apart can be used (see 4 and 5 in figure 4), if the error caused by the slope is small.
2. Elevation change can be determined by comparison of DEMs derived from different GLAS campaigns (Slobbe *et al*. 2008). GLA12 provides precise information on horizontal location and elevation data so that a DEM can be produced; the grid size of the DEM can be $0.1° \times 0.1°$. Changes can be derived from the latest DEM by subtracting an earlier one. This method takes one DEM as a reference surface. Therefore, GLAS data acquired during different campaigns can be used. However, the precision of change detection depends on having a high density of footprints in each grid, and this method is not effective at lower latitudes where the distribution of laser footprints is sparse. At the same time, slope-induced errors are difficult to quantify over areas that are not flat since footprints from different campaigns may differ largely in horizontal location.
3. Elevation change can be determined from comparison of crossover elevation. In order to make the best use of GLAS data, different orientation data can be used to extract elevation changes if there are no overlapping footprints (see 2 and 3 in figure 4). Firstly, crossovers should be located. Secondly, for each track, the adjacent data are used to fit a linear trend so that the data can be interpolated to give the elevation at the crossover point, assuming that the surface is continuous. The crossover elevation can be interpolated with the adjacent elevation from both sides along a track (e.g. Smith *et al*. 2005, Brenner *et al*. 2007). Thirdly, elevation changes are derived by subtracting the elevation of the previous track from that of the subsequent track. Information about crossover density at different latitudes is shown in table 4 (Schutz 1998) if the ICESat/GLAS adopted the 183-day repeat track.

These methods have been widely used since the production of GLAS data. For these three methods, (1) and (3) are always combined to detect changes in elevation. Shuman *et al*. (2006) presented the primary precision (about 2.1 cm) and accuracy (about ±14 cm) of selected elevation data (Release 21) from 2003 to 2004 based on crossover differences. In addition, factors affecting change detection of elevation were discussed and the location of ice-shelf grounding lines from ICESat/GLAS data was suggested to be derived based on the distinction between ground and floating areas.

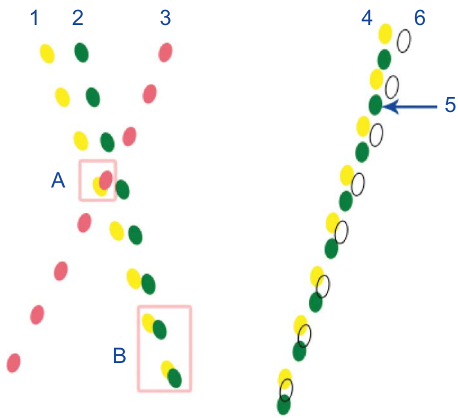

Figure 4. Sketch map of crossovers for GLAS. Area A and Area B in the boxes show cross-track overlapping footprints and repeat-track overlapping footprints, respectively. There are no overlapping footprints between track 2 and track 3, although a crossover point does exist.

Table 4. Number of crossovers in 100 km × 100 km for ICESat/GLAS 183-day repeat track.

Latitude ranges	Number of crossovers
70°–71°	230
75°–76°	550
80°–81°	1675
84°–85°	11500

Fricker and Padman (2006) located the ice-shelf grounding line by change analysis of repeat-track elevation from 2003 to 2006 in the Institute Ice Stream region of the southern Ronne Ice Shelf because the data at different phases of the ocean tide can help determine the landward and seaward limits; they demonstrated that the location of the grounding zone based on feature identification in satellite imagery or DEMs may be in error by several kilometres for their coarse resolutions. Rignot and Kanagaratnam (2006) discussed the weakness in elevation change detection assuming a smooth surface using GLAS data. Subglacier water system information was successfully extracted from variation of repeat-track elevation from GLAS data in the Antarctic plateau (Fricker *et al*. 2007). Slobbe *et al*. (2008) gave an estimation of volume change rates of Greenland's ice sheet using ICESat overlapping footprints. Most change-detection methods use only a small part of the data, such as overlaps and crossovers. How to make the best use of GLAS data from each campaign requires further investigation.

3.3 *Measurements of land elevation and forest height*

Global change has attracted a great deal of research attention in recent years. Greenhouse gases such as CO_2 and CH_4, have become a great concern all over the world (Patenaude *et al*. 2005). Forest lands play an important role in the global carbon cycle, by exchanging CO_2 with the atmosphere through photosynthesis and respiration (e.g. Dixon *et al*. 1994, Patenaude *et al*. 2005, Stewart and Hessami 2005). Three-dimensional (3D) information on forest canopies is a critical source of information for biomass estimation and the determination of local carbon budgets (Gong *et al*. 1999, 2000). Information on the vertical distribution of forest and shrubs is badly needed for forest ecosystem dynamics. With multi-spectral and hyperspectral remote sensing or even with aerial photography, the horizontal distribution of vegetation can be derived and species can also be interpreted (Gong *et al*. 2001). Although 3D information can be derived from photogrammetry and Synthetic Aperture Radar (SAR) interferometry (Gong *et al*. 2002, Brown *et al*. 2010, Neumann *et al*. 2010), the information is mostly concerned with the surface of the canopy. With the improvement of altimetry technology, especially when LiDAR came into use, LiDAR altimetry data contain the most direct measurements of forest structural information, including the height of the canopy and the height of the understorey vegetation and biomass. Different airborne LiDAR instruments, such as the Scanning LiDAR Image of Canopies by Echo Recovery (SLICER) and the Laser Vegetation Imaging Sensor (LVIS), as well as commercial airborne LiDAR instruments have been widely used (e.g. Blair *et al*. 1999, Lefsky *et al*. 1999a,b, Dubayah and Drake 2000, Weishampel *et al*. 2000, Harding *et al*. 2001, Drake *et al*. 2002, Chen *et al*. 2007, Huang *et al*. 2009). These instruments are powerful for vegetation-height extraction at the local and regional scale. When ICESat/GLAS was launched in 2003 with the first spaceborne laser system, it started to play a role in global forest-height retrieval.

GLA01 data and GLA14 data are usually combined to derive vegetation height (Duong *et al*. 2007, Lefsky *et al*. 2007, Pang *et al*. 2008), which can be matched by the record index, since the waveform information is recorded in GLA01 data and GLA14 data have horizontal geographical coordinates and other parameters. For each GLAS waveform, there are 544 bins (one bin corresponds to 1 ns or 15 cm), with a range capability of 81.6 m. From campaign L3a, the bin size from 1 to 151 changed to 60 cm, and other bins remained unchanged, so that the range capability was expanded to 150 m (Harding and Carabajal 2005, Sun *et al*. 2008).

Since the 1064 nm laser pulse, whose waveform can be described by a single peak Gaussian equation, is used to do altimetry measurements, the echo waveform will also be a single peak Gaussian function if the footprints are located over flat areas. However, in forested areas, the received laser pulse waveforms usually contain several peaks as the combination of several Gaussian functions corresponding to returns from different layers in the forest; in particular, from the top layer first and the ground, see figure 5 (for GLA14 data, at most six alternate different Gaussian functions can be separated from the return laser waveform). Thus, the height of the canopy can be determined by analysing the return waveforms (Brenner *et al*. 2003). For return laser waveforms, the mean and standard deviation of background noise can first be calculated from waveform data. Signal start time and end time can be determined by a threshold, such as three standard deviations above the mean noise value (Sun *et al*. 2008). De-noise processing is then applied to the original waveform. Next, waveform decomposition is used to fit each peak. The signal start time always corresponds to the top layer, and the location of the last peak stands for the ground (Hofton *et al*. 2000, Neuenschwander *et al*. 2008) (see figure 5, signal start line (black) corresponding to forest-top layer in the footprint and the location of last peak (black line) corresponding to the ground elevation). Therefore, taking the time period between the signal start and the last peak, multiplying by the speed of light and dividing by two gives the vegetation height, see figure 5.

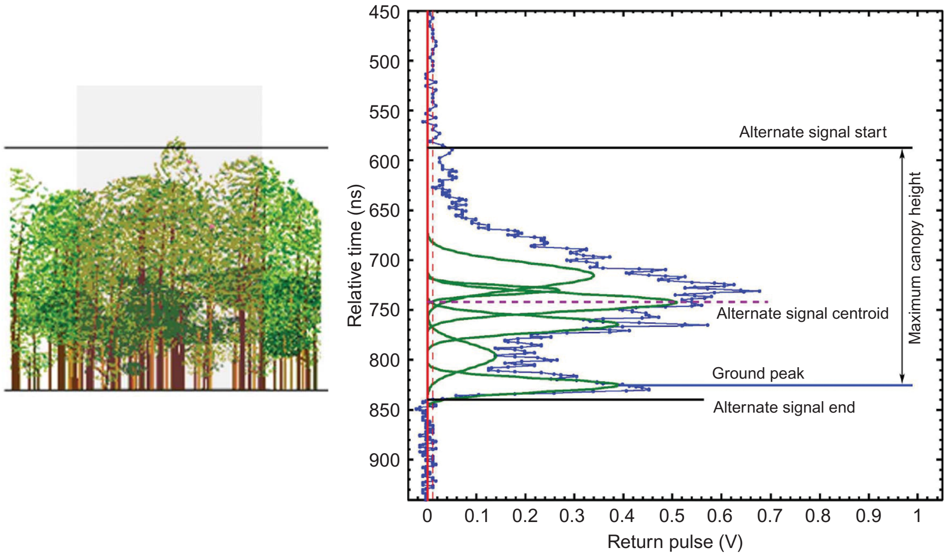

Figure 5. GLAS return pulse after interacting with the forest. The blue points are return echo samples. The standard deviation is indicated by a red dashed line. The mean of the noise is indicated as a red line. The horizontal black lines represent the signal start and end times. GLA14 alternate decomposed Gaussian equations are depicted by green lines, and the location of the signal start and end times are depicted as separate black lines. The alternate signal centroid is given as a purple dashed line. The location of the last peak (blue horizontal line) stands for ground, and the maximum canopy height is indicated as a vertical black line.

However, there are still some critical issues requiring further research. Forest-height determination over sloping areas is a big challenge since the variation in ground elevation results in a coarse ground height when derived from received waveforms, especially in mountainous areas. The exact ground height corresponding to the tip of the tree top is hard to locate given that the GLAS footprint is much greater than a tree canopy in area, although different models have been developed to describe this (Gwenzi 2008). The ground elevation is difficult to determine since signals from both the ground and low shrub are often mixed together (Rosette *et al*. 2008, Chen 2010a). For mountainous areas, different regression models have been developed to consider slope information within a GLAS illuminating footprint because signals induced by slope, which can be derived from local DEMs need to be removed from metrics in order to extract an accurate forest height (Lefsky *et al*. 2005, Rosette *et al*. 2008). Thus, the analysis of waveform leading edges and trailing edges (Lefsky *et al*. 2007) is essential. However, regression models differ for different sites. In addition, the algorithm to specify the threshold of the signal is not consistent. Waveform decomposition techniques need to be further developed especially for these complicated areas. In addition to canopy-height determination, above-ground biomass estimation with a statistical model from forest maximum height (Simard *et al*. 2008) is another important application.

GLAS data application in forested area has been carried out in recent years by a number of researchers. Harding and Carabajal (2005) modified the waveform with an instrument model according to a high-resolution DEM, and then compared it with the actual waveform of GLAS; they confirmed that the extraction of biophysical parameters over tree-covered areas of low relief can be accomplished with ICESat data. Lefsky *et al*. (2005) extracted maximum forest height in tropical broadleaf forests, temperate broadleaf forests and temperate needleleaf forests using GLAS waveform data and a knowledge of local topography, as well as an above-ground biomass estimation with an empirical method. Sun *et al*. (2008) reported forest-height extraction over a forested area in the USA using GLAS data from autumn 2003 to summer 2005 and airborne LVIS data. Forest heights determined from these two types of data were in good agreement. Dolan *et al*. (2009) derived forest growth rate from GLAS data and Landsat-based disturbance history maps in three regions of the USA, as well as the estimation of above-ground wood productivity from height–biomass allometric relations. Chen (2010b) used GLAS data to extract forest canopy height over mountainous areas (with mean slope of around 20°) and pointed out that the direct canopy height from GLAS waveform metrics tended to be higher than that derived from airborne LiDAR data and that it was difficult to identify signal start time and terrain ground elevation. Lefsky (2010) estimated forest heights over the world with Moderate Resolution Imaging Spectroradiometer (MODIS) data determining the forest-covered areas and GLAS data estimating height.

3.4 *Measurements of cloud and aerosol vertical distribution and optical depth derivation*

Cloud feedback and the influence of aerosol are considered as major uncertainties for predictions of global climate (Spinhirne *et al*. 2005a). In addition, knowledge on the height, coverage and thickness of cloud layers is essential in modelling the radiative fluxes at the surface and within the atmosphere (Palm *et al*. 2002). Spaceborne radiometers and imagers could give a direct view of cloud tops, but the vertical distribution of clouds could not be easily and reliably derived from them. Efforts have been taken to study the structure of clouds and aerosols. Different LiDAR systems have been developed, such as the Cloud and Aerosol LiDAR System, the Cloud-aerosol LiDAR with Orthogonal Polarization and the LiDAR In-space Technology Experiment (Berthier and Toutin 2008). As a first polar-orbit laser sensor, GLAS could be able to monitor more southern and more northern areas to provide data for polar climate research.

Since GLAS is a dual-frequency laser system, it can provide atmospheric profiling at both 532 nm and 1064 nm, which use photon-counting detectors and analogue detection, respectively (Yang *et al*. 2008). The detailed characteristics of the two channels are listed in table 5. The 1064 nm channel, with an Avalanche photodiode detector with a 0.1 mm band-pass filter and a 450 μrad field of view (Palm *et al*. 2002), can be used to detect the cloud height, and the 532 nm channel, with a tight band-pass filter of about 30 pm and a field of view of about 150 μrad, relying on photon-counting detectors (McGill *et al*. 2005), can be used to detect vertical structures of aerosols and thin clouds (e.g. Shiobara *et al*. 2004, Spinhirne *et al*. 2004, 2005a,b). The 1064 nm channel will supplement when and if the 532 nm channel is saturated since the backscatter from dense clouds is strong.

Table 5. Characteristics of two channels (Palm *et al*. 2002).

Parameter	532 nm channel	1064 nm channel
Laser energy (mJ)	36	73
Laser divergence (μrad)	110	110
Laser repetition rate (Hz)	40	40
Receiver field of view (μrad)	150	450
Detector dark current (A)	3.0×10^{-16}	50.0×10^{-12}
Detector quantum efficiency	60%	35%
RMS detector noise	0.0	2.0×10^{-11}
Electrical bandwidth	1.953×10^{6}	1.953×10^{6}
Optical filter bandwidth (nm)	0.030	0.080
Total optical transmission (%)	30	55

3.4.1 Measurements of cloud-top layer height and aerosol vertical distribution. The transmitted laser pulse interacts with molecular, aerosol, cloud and other particles and finally is received by the detector of the receiver detector. This process can be described by the standard LiDAR equation. Then, aerosol extinction coefficient and backscatter coefficient can be obtained:

$$P(z) = P_0 \frac{cT_s}{2} A(\beta_\pi(z)/z^2) \exp[-2\int_0^r \sigma(z')\mathrm{d}z'] + P_b + P_d, \tag{7}$$

where $P(z)$ is the power of the back-scattered laser pulse at an altitude of z, P_0 is the power of the transmitted laser pulse, c is the speed of light, $\sigma(z')$ and $\beta_\pi(z)$ are the extinction coefficient and backscatter coefficient, respectively, at the altitude of z, T_s is the time for a single laser pulse, A is the area of the laser receiver, P_b is the scattered solar radiation and P_d is the detector dark signal.

With equation (7), after applying fundamental corrections and normalizations to the raw LiDAR signal, the normalized LiDAR signal $P'(z)$ is generated and stored in GLA02 data. In addition, if the LiDAR calibration constant C is calculated, the calibrated attenuated backscatter cross section $\beta'(z)$ is easy to obtain from the normalized LiDAR signal. For the 1064 nm channel, the calibrated attenuated backscatter cross section is obtained by (Palm *et al*. 2002):

$$\beta'(z) = P'(z)/C. \tag{8}$$

Figure 6 depicts the back-scattered energy distribution for the 532 nm signal for GLA07 data. Aerosol and cloud-layer-height data are designated as GLA09, and the layer-detection algorithm is a single-pass threshold comparison technique designed for use with the 532 nm data. First, in order to increase the signal to noise ratio (SNR), a time series of GLAS profiles in 4 s segments will be combined to calculate an averaged attenuated backscatter coefficient profile. In addition, the corresponding threshold profile is obtained by computing Rayleigh backscatter values. In clear regions, radiative scattering stems entirely from Rayleigh scattering and when particles are present, scattering is increased (Palm *et al*. 2002). A layer boundary-detection algorithm is based on the backscatter coefficient profile comparison with the threshold profile in the vertical direction. If a specified number of consecutive bins exceed the

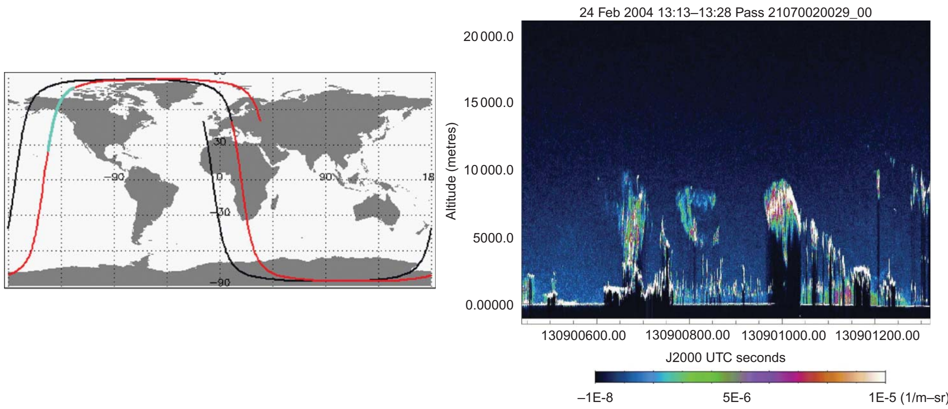

Figure 6. Backscatter cross-section distribution in 532 nm for GLA07 data (descending), ICESat was travelling from the north of America to the Pacific Ocean, as depicted by the cyan line in the left panel, and the red line depicts the actual ground track.

threshold, a layer top is assigned to that position. A layer bottom is assigned to where the signal magnitude of a number of consecutive bins falls below the threshold value (Breón *et al*. 2005, Hart *et al*. 2005). Thus, both the top and the bottom of a layer are determined. Specifically, the layer boundary is the first two bins exceeding or falling below the appropriate threshold based on molecular scattering (Dessler *et al*. 2006). This algorithm to define a layer is used to find boundaries of both cloud and aerosol layers. The threshold algorithm with two or three bins to define a cloud layer was discussed by Mahesh *et al*. (2004), and approximately 4% more layers were detected using two bins as a threshold. In order to assign a type to a layer, it will be necessary to test it to determine how well it matches characteristics ascribed to cloud and aerosols. The signal magnitude, signal gradient and altitude of the top of each layer are used in the layer discrimination procedure to indicate the likelihood that a layer is either cloud or aerosol (Palm *et al*. 2002).

3.4.2 Optical depth derivation. The most important optical characteristic obtained from the LiDAR backscatter profile is particle optical depth. For aerosols, the optical depth can be derived from:

$$\sigma(z) = S_{\mathrm{p}}\beta'(z) \tag{9}$$

and

$$\tau = \int_{z_{\mathrm{t}}}^{z_{\mathrm{b}}} \sigma(z')\mathrm{d}z', \tag{10}$$

where S_{p} is the aerosol extinction to backscatter ratio or LiDAR ratio, which can be obtained through a look-up table, z_{t} and z_{b} are top and bottom of a specific layer and τ is the optical depth. For cloud, the optical depth derivation is also based on equations (9) and (10), but the process is more complicated. The method to derive cloud optical depths of dense clouds was discussed by Yang *et al*. (2008), and the critical issue was to calibrate solar background signals (it was always considered as

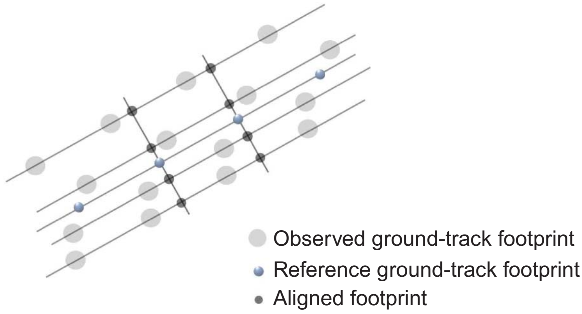

Figure 7. Repeat tracks and aligned points (redrawn from Yi *et al*. 2005).

noise before), since this part needs to be subtracted from signals received by the photon detectors.

Many researchers have contributed to the application of GLAS aerosol and cloud data. Spinhirne *et al*. (2005a) presented an example of GLAS data usage in profiling significant cloud and aerosol layers in the atmosphere and, from that, we can see the 532 nm channel has a higher SNR than the 1064 nm channel. Dessler *et al*. (2006) determined the heights of different cloud layers by analysing GLAS data from the tropics. Hlavka *et al*. (2005) verified the precision of cloud and aerosol depth data derived from GLAS data by comparing with Cloud Physics LiDAR (CPL) data. To visualize GLAS data, a software package, named the Interactive Data Language (IDL) Visualizer (ICESAT/GLAS Science Computing Team 2008), is available from NSIDC, and this enables the direct distribution of cloud and aerosol to be examined visually.

3.5 *Ice-sheet slope extraction*

Ice-sheet slope and roughness are mainly affected by bedrock topography, ice flow, ice thickness, wind and mass balance. In polar areas, accurate slope information can be used to improve the accuracy of both radar altimeter and laser altimeter elevation measurement because slope-induced error in GLAS footprints can be calculated accurately. During the operation of ICESat/GLAS, millions of sets of altimetry data were obtained. In areas with constant slope, the slope information within a footprint can be obtained because the returned waveform is broadened after interacting with a sloped surface (Brenner *et al*. 2003). For large areas, slope information can also be achieved by analysing GLAS repeat-track data. Yi *et al*. (2005) gave an algorithm to extract the 3D surface slope information using the repeat ground-track elevation data, and the process is summarized below.

Firstly, filter the altimetry data to avoid those affected by cloud or reflected from cloud. Secondly, altimetry data are selected according to different repeat tracks and a reference ground track (bright blue circles in figure 7) can be selected to align the other repeat tracks. Thirdly, align points in other repeat tracks to the points in the reference ground track. A reference footprint is selected and then a line perpendicular to the reference track is drawn. Thus, the intersections can be located (small dark circles in figure 7). Fourthly, calculate the elevation of those intersections. Two adjacent laser footprints are used to fit a linear trend so the intersection along track can be interpolated. Fifthly, calculate the slope in both along-track and cross-track directions:

$$\tan s = \Delta h / D, \tag{11}$$

where s is the slope, Δh is the height difference between two adjacent altimetry data and D is the distance of these two footprints.

Finally, the 3D slope can be obtained by combining the along-track slope and cross-track slope:

$$\tan^2 S = \tan^2 s_a + \tan^2 s_c, \tag{12}$$

where S is the 3D slope, s_a is the along-track slope and s_c is the cross-track slope.

However, an error could be introduced in the process mentioned above. Even with the ICESat/GLAS data from the same campaign, the exact data collection time is not the same, and the elevation may be changed over time. In addition, the accuracy of horizontal location and altimetry accuracy are critical to the slope information extraction. More detailed information was given by Yi *et al*. (2005).

3.6 *Land-cover classification*

Land cover is one of the most important applications in remote sensing and different kinds of remotely sensed images are used for land-cover classification. However, the data from the satellite laser altimeter ICESat/GLAS can also be used for land-cover classification. ICESat/GLAS makes three basic measurements (Brenner *et al*. 2003): (1) the range from the laser to the nadir surface; (2) the shape of the returned laser waveform, which is reflected from different surfaces; and (3) the returned laser pulse energy, which is affected by the reflectivity of the medium. These measurements can be combined to carry out land-cover classification. Duong *et al*. (2006) gave an example of land-cover classification in the Netherlands and four categories were obtained: high vegetation, urban, water and bare land/low vegetation. The method is summarized below.

Returned laser waveform data and energy data are used in the process. Firstly, the original laser waveform is normalized and the normalized waveform is smoothed. Secondly, a waveform decomposition technique is used to derive all the Gaussian components in the processed waveform. This is similar to what was discussed in section 3.3. The background signal can be calculated and the signal start time and end time are located. Three parameters are provided in this step: the number of Gaussian components (N), the location of the signal start (S) and the width of the signal start and signal end (W). Thirdly, land cover is classified with a decision-tree algorithm (a flow chart of this algorithm can be seen in figure 8). N, S, W and waveform energy (E), which is relevant to the land-surface reflectance, are used by the classification algorithm. The algorithm is based on the land covers and their laser response analysis. For water, the reflectance is small so that the returned waveform energy E is lower than that of the other three. A threshold can be set to derive water. Then, N is used to derive bare land because bare surfaces usually correspond to only one Gaussian component. W and N can also be combined to derive bare land with small trees or low vegetation and multi-Gaussian components occurred in the waveform since the W is narrower and the N is less than high trees and buildings. Signals from high vegetation correspond to a wider first signal mode (corresponding to an earlier signal start

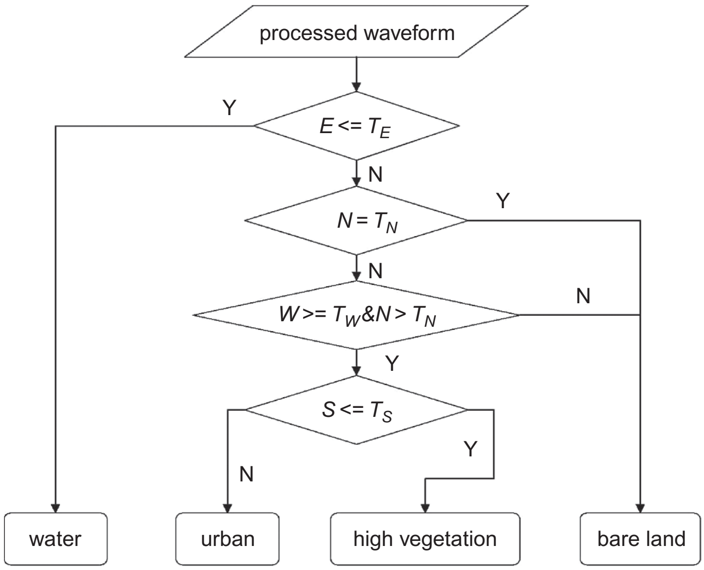

Figure 8. Flow chart of land-cover classification (adapted from Duong *et al.* 2006). T_E, T_N, T_S and T_W are the thresholds of E, N, S and W.

time S) than urban and multi-Gaussian components, and they can be differentiated by S. Finally, the classification result from ICESat/GLAS is validated with different land-cover maps.

Duong *et al.* (2006) classified these four different land-cover types with an accuracy of approximately 73%, and the algorithm was not good enough to differentiate water and bare land. The method can be improved. By comparison of the width of every single Gaussian component, better classification results of urban and high buildings can be derived. More detailed information can be found in Duong *et al.* (2006). However, in polar areas, the land-cover classification is not the same as that discussed above. This is because in polar areas, the land cover is mainly snow, ice, rocks and water. Molijn *et al.* (2011) gave an example of land-cover classification in the Dry Valleys of Antarctica with an algorithm of a decision tree, which are composed of kurtosis, reflectivity, width and saturation information of waveforms with an overall classification accuracy of 74%.

3.7 *Urban building height extraction*

Urban expansion monitoring is an important application of remote sensing. Urban building heights can be derived from digital photogrammetry, interferometric synthetic aperture radar (InSAR) and airborne LiDAR (Alexander *et al.* 2009, Cheuk and Yuan 2009, Meng *et al.* 2009, Sauer *et al.* 2009). ICESat data can also be used to extract urban building height. The LiDAR returned waveform is composed of various signals from different layers, and a typical urban area scene is shown in figure 9. The final waveform is relevant to the height levels, roof reflectance, roof slope, roof area and ground structure in the footprint. Gong *et al.* (2011) gave the first example of building height extraction using GLAS data and the method is summarized below.

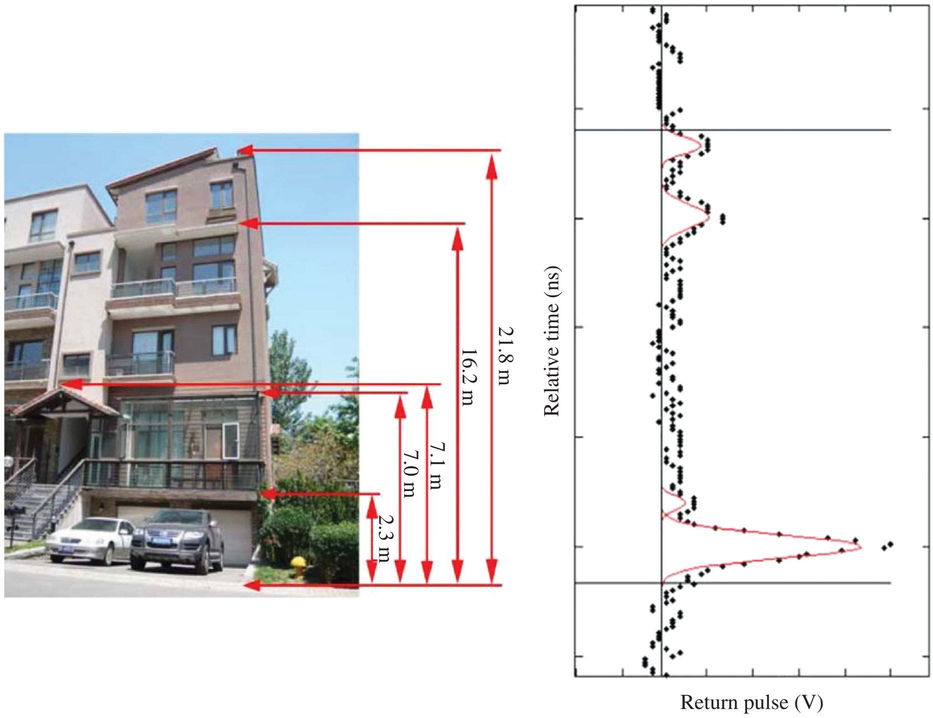

Figure 9. Different building height layers and corresponding laser waveform. The two horizontal black lines show the location of the signal start and end, and the red lines show the decomposed Gaussian peaks.

Firstly, GLA01 original waveform data are selected and the de-noising and smoothing processing is carried out, which is similar to that discussed in section 3.3. Secondly, waveform decomposition is used to fit the processed waveform, and the signal start, signal end and different Gaussian components can be recorded. Thirdly, the decomposed Gaussian components are used to extract building height. The earliest decomposed Gaussian function (FM) corresponds to the tallest target in the footprint and the latest one (LM) corresponds to ground. Therefore, the maximum building height within a footprint should be calculated from:

$$\mathrm{MBH} = c(t_{\mathrm{c,LM}} - t_{\mathrm{c,FM}})/2, \tag{13}$$

where MBH is the maximum building height, c is the speed of light and $t_{\mathrm{c,LM}}$ and $t_{\mathrm{c,FM}}$ are the centre position of the LM and FM, respectively. Fourthly, extracted building height from ICESat/GLAS can be validated with *in situ* measured building height.

With this method, Gong *et al*. (2011) extracted some building heights in Beijing with a root mean squared error of 6.4 m. Compared with the result from a direct use of GLA14 Gaussian extraction, this method is more accurate. They pointed out that accurate discrimination of building roofs and tree canopies can help improve building height extraction. More detailed information is given by Gong *et al*. (2011). In addition, the total floor space of buildings can be obtained by combining GLA14 data with land-use/land-cover data (Cheng *et al*. 2011).

3.8 *Changes in glaciers and ice caps*

Dynamic change of ice caps and glaciers is closely related to global climate change and sea-level changes. Changes in the extent of ice caps or glaciers can be derived from traditional remote-sensing images. Changes in volume can be estimated if information about the elevation changes can be obtained. For their smaller area compared with ice sheets, change-detection methods for ice caps or glaciers are slightly different from that discussed in section 3.2. The altimetry data from ICESat/GLAS can provide highly accurate changes at the footprint compared with an existing DEM in the ice-cap and glacier regions. The process is summarized below.

Firstly, a DEM in the study area that is already developed is needed as the reference data. A DEM derived from stereoscopic pairs of Terra-Advanced Spaceborne Thermal Emission and Reflection Radiometer (ASTER), Système Probatoire d'Observation de la Terre5-High Resolution Geometric (SPOT5-HRG) and Advanced Land Observing Satellite–Panchromatic Remote-Sensing Instrument for Stereo Mapping (ALOS–PRISM) or a Shuttle Radar Topography Mission (SRTM) Digital Elevation Model (DEM) can be used as a reference surface (Sauber *et al*. 2005, Berthier and Toutin 2008, Kääb 2008, Sneed *et al*. 2008). Secondly, ICESat/GLAS data are selected and filtered to avoid cloud effects. Thirdly, height difference can be obtained by subtracting the reference height with GLAS altimetry data. For some small glaciers, there may be only a few tracks of data covering them. However, the availability of these data can make it a promising tool for investigating regional-scale volume changes of glaciers (Kääb 2008).

3.9 *Water-level changes in lakes*

Water levels in a lake can be considered as having the same altitude at a specific time. Therefore, the laser altimetry data over different areas over the lake in different campaigns can be used to study water-level changes. In arid areas, without *in situ* hydrological measurements, GLAS data can be an effective alternative to water-level monitoring. Chipman and Lillesand (2007) obtained lake-level changes from GLAS data in southern Egypt from 2003 to 2005, and Urban *et al*. (2008) examined water-level changes from ICESat/GLAS data with local tide-gauge data in Lake Pontchartrain, Louisiana, USA. The method is summarized below.

Firstly, laser altimetry data unaffected by cloud over a lake area are selected, and saturation correction is carried out to those saturated footprints for the high laser echoes. The reason for saturation correction is that a saturated waveform corresponds to a lower elevation than the actual values (Urban *et al*. 2008). Secondly, water-level slope is calculated and removed along ICESat tracks. For the limited accuracy geoid model, the altimetry data along track can depict a sloped surface that needs to be removed to get an accurate lake water level. Thirdly, altimetry data from different times are averaged to get the lake water level. Thus, averaged lake water levels in different campaigns are comparable, and the lake water-level variation is clear.

The result shows that the lake water-level change obtained with this method agrees well with that from tide-gauge data (Urban *et al*. 2008). However, the limited observation schedule each year could not supply enough data for hydrological applications.

4. Conclusion

GLAS data is widely used in various fields, and many important discoveries have been made, such as subglacier water system extraction, Greenland and Antarctic ice-sheet variation, global forest-height distribution, etc. The application of GLAS data is not limited to the areas reviewed above. Although successful examples are constantly being produced, there are many issues limiting its use in Earth science studies. The low density of GLAS footprints does not completely produce a wall-to-wall mapping of the Earth's surface; this is a particularly limiting factor in the lower latitudes. Nonetheless, as the technology of satellite laser altimetry continues to advance, the potential of global laser measurement can be expanded to more application fields of science. Presently, ICESat/GLAS has already stopped working, and ICESat-2 is scheduled to be launched in 2015 with a broader application than its predecessor (Abdalati *et al*. 2010).

Acknowledgements

We would like to give special thanks to Professor Arthur Cracknell and other reviewers for their constructive suggestion and all their efforts to improve this paper. Also we thank the National Snow and Ice Data Center for distributing ICESat data and providing the data processing software, IDL Visualizer. This research is partially supported by grants from the National High Technology Research and Development Program of China (863 program) (grant no. 2008AA09Z117 and grant no. 2008AA121702), an NSF Biocomplexity Grant (grant no. NSF DEB 04-21530) and the National High Technology Program of China (grant no. 2009AA12200101).

References

Abdalati, W., Zwally, H.J., Bindschadler, R., Csatho, B., Farrell, S.L., Fricker, H.A., Harding, D., Kwok, R., Lefsky, M., Markus, T., Marshak, A., Neumann, T., Palm, S., Schutz, B., Smith, B., Spinhirne, J. and Webb, C., 2010, The ICESat-2 Laser Altimetry Mission. *Proceedings of the IEEE*, **98**, pp. 735–751.

Abshire, J.B., Sun, X., Riris, H., Sirota, J.M., McGarry, J.F., Palm, S., Yi, D. and Liiva, P., 2005, Geoscience Laser Altimeter System (GLAS) on the ICESat Mission: on-orbit measurement performance. *Geophysical Research Letters*, **32**, L21S02, doi:10.1029/2005GL024028.

Alexander, C., Smith-Voysey, S., Jarvis, C. and Tansey, K., 2009, Integrating building footprints with LiDAR elevation data to classify roof structures and visualize buildings. *Computers, Environment and Urban Systems*, **33**, pp. 285–292.

Allan, G.R., 2008, Evidence for optically induced heating of the GLAS/ICESAT doubler crystal. In *Proceedings IEEE LEOS Annual Meeting*, 4–9 May 2008, San Jose, CA, pp. 216–217.

Alley, R.B., Clark, P.U., Huybrechts, P. and Joughin, I., 2005, Ice-sheet and sea-level changes. *Science*, **310**, pp. 456–460.

Bae, S.K. and Schutz, B.E., 2002, Precision attitude determination, algorithom theoretical basis document, Version 2.2 (Greenbelt, MD: NASA Goddard Space Flight Center).

Bamber, J.L., Riva, R.E.M., Vermeersen, B.L.A. and Lebrocq, A.M., 2009, Reassessment of the potential sea-level rise from a collapse of the West Antarctic ice sheet. *Science*, **324**, pp. 901–903.

Benoit, L., Fabrice, P., Frederique, R., Gaetan, V., Mathias, V.D.B. and Ouan-Zan, Z., 2005, ENVISAT radar altimeter measurements over continental surfaces and ice caps using the ICE-2 retracking algorithm. *Remote Sensing of Environment*, **95**, pp. 150–163.

BERRY, P.A.M., 2000, Topography from land radar altimeter data: possibilities and restrictions. *Physics and Chemistry of the Earth, Part A, Solid Earth and Geodesy*, **25**, pp. 81–88.

BERTHIER, E. and TOUTIN, T., 2008, SPOT5-HRS digital elevation models and the monitoring of glacier elevation changes in north-west Canada and south-east Alaska. *Remote Sensing of Environment*, **112**, pp. 2443–2454.

BLAIR, J.B., RABINE, D.L. and HOFTON, M.A., 1999, The laser vegetation imaging sensor (LVIS): a medium-altitude, digitations-only, airborne laser altimeter for mapping vegetation and topography. *ISPRS Journal of Photogrammetry and Remote Sensing*, **54**, pp. 115–122.

BRENNER, A.C., DIMARZIO, J.P. and ZWALLY, H.J., 2007, Precision and accuracy of satellite radar and laser altimeter data over the continental ice sheets. *IEEE Transactions on Geoscience and Remote Sensing*, **45**, pp. 321–331.

BRENNER, A.C., ZWALLY, H.J., BENTLEY, C.R., CSATHÓ, B.M., HARDING, H.J., HOFTON, M.A., MINSTER, J.B., ROBERT, L.A., SABA, J.L., TOMAS, R.J. and YI, D.H., 2003, Derivation of range and range distributions from laser pulse waveform analysis for surface elevations, roughness, slope and vegetation heights, Algorithm theoretical basis document, Version 4.1 (Greenbelt, MD: NASA Goddard Space Flight Center).

BREÓN, F.M., O'BRIEN, D.M. and SPINHIRNE, J.D., 2005, Scattering layer statistics from space borne GLAS observations. *Geophysical Research Letters*, **32**, L22802, doi:10.1029/2005GL023825.

BRITTINGHAM, L.C. and LEE, J., 2005, GLAS standard data products specification – level 2 version 8. Available online at: http://glas.wff.nasa.gov/files/documents/gsas_prod_spec_2_v8.pdf (accessed 11 May 2010).

BROWN, C.G., SARABANDI, K. and PIERCE, L.E., 2010, Model-based estimation of forest canopy height in red and Austrian pine stands using Shuttle Radar Topography Mission and ancillary data: a proof-of-concept study. *IEEE Transactions on Geoscience and Remote Sensing*, **48**, pp. 1105–1118.

CAVALIERI, D.J. and MARKUS, T., 2006, EOS Aqua AMSR-E Arctic sea-ice validation program: Arctic 2006 aircraft campaign flight report. NASA/TM-2006-214142 (Greenbelt, MD: Goddard Space Flight Center).

CHAMBERS, D.P., 2007, Gravimetric methods – spacecraft altimeter measurements. *Treatise on Geophysics*, **3**, pp. 123–161.

CHEN, Q., 2010a, Assessment of terrain elevation derived from satellite laser altimetry over mountainous forest areas using airborne LiDAR data. *ISPRS Journal of Photogrammetry and Remote Sensing*, **65**, pp. 111–122.

CHEN, Q., 2010b, Retrieving vegetation height of forests and woodlands over mountainous areas in the Pacific Coast region using satellite laser altimetry. *Remote Sensing of Environment*, **114**, pp. 1610–1627.

CHEN, Q., GONG, P., BALDOCCHI, D. and TIAN, Y., 2007, Estimating basal area and stem volume for individual trees from LiDAR data. *Photogrammetric Engineering and Remote Sensing*, **73**, pp. 1355–1365.

CHENG, F., WANG, C., WANG, J.L., TANG, F.X. and XI, X.H., 2011, Trend analysis of building height and total floor space in Beijing, China, using ICESat–GLAS data. *International Journal of Remote Sensing*.

CHEUK, M.L. and YUAN, M., 2009, Assessing spatial uncertainty of LiDAR-derived building model: a case study in downtown Oklahoma city. *Photogrammetric Engineering and Remote Sensing*, **75**, pp. 257–270.

CHIPMAN, J.W. and LILLESAND, T.M., 2007, Satellite based assessment of the dynamics of new lakes in southern Egypt. *International Journal of Remote Sensing*, **28**, pp. 4365–4379.

CLARK, P.U., ALLEY, R.B. and POLLARD, D., 1999, Northern hemisphere ice-sheet influences on global climate change. *Science*, **286**, pp. 1104–1111.

CONNOR, L.N., LAXON, S.W., RIDOUT, A.L., KRABILL, W.B. and MCADOO, D.C., 2009, Comparison of Envisat radar and airborne laser altimeter measurements over Arctic sea ice. *Remote Sensing of Environment*, **113**, pp. 563–570.

COOPER, A.P. R. and HINTON, J.C., 1996, Correction of satellite radar altimeter data on ice-covered surfaces in Antarctica using an integrated geographical information system. *International Journal of Remote Sensing*, **17**, pp. 1367–1376.

CUDLIP, W. and MILNES, M., 1994, Overview of altimeter data processing at the U.K. Earth Observation Data Centre. *International Journal of Remote Sensing*, **15**, pp. 871–887, doi: 10.1080/01431169408954122.

DESSLER, A.E., PALM, S.P. and SPINHIRNE, J.D., 2006, Tropical cloud-top height distributions revealed by the Ice, Cloud, and Land Elevation Satellite (ICESat)/Geoscience Laser Altimeter System (GLAS). *Journal of Geophysical Research*, **111**, D12215, doi:10.1029/2005JD 006705.

DIMARZIO, J., BRENNER, A., SCHUTZ, R., SHUMAN, C.A. and ZWALLY, H.J., 2007a, *GLAS/ICESat 500 m Laser Altimetry Digital Elevation Model of Antarctica* (Boulder, CO: National Snow and Ice Data Center).

DIMARZIO, J., BRENNER, A., SCHUTZ, R., SHUMAN, C.A. and ZWALLY, H.J., 2007b, *GLAS/ICESat 1 km Laser Altimetry Digital Elevation Model of Greenland* (Boulder, CO: National Snow and Ice Data Center).

DIXON, R.K., BROWN, S., HOUGHTON, R.A., SOLOMON A.M., TREXLER, M.C. and WISNIEWSKI, J., 1994, Carbon pools and flux of global forest ecosystems. *Science*, **263**, pp. 185–190.

DOLAN, K., MASEK, J.G., HUANG, C. and SUN, G., 2009, Regional forest growth rates measured by combining ICESat GLAS and Landsat data. *Journal of Geophysical Research*, **114**, G00E05, doi:10.1029/2008JG000893.

DRAKE, J.B., DUBAYAH, R.O., CLARK, D.B., KNOX, R.G., BLAIR, J.B., HOFTON, M.A., CHAZDON, R.L., WEISHAMPEL, J.F. and PRINCE, S., 2002, Estimation of tropical forest structural characteristics using large footprint LiDAR. *Remote Sensing of Environment*, **79**, pp. 305–319.

DUBAYAH, R.O. and DRAKE, J.B., 2000, LiDAR remote sensing for forestry. *Journal of Forestry*, **98**, pp. 44–46.

DUONG, H., LINDENBERGH, R., PFEIFER, N. and VOSSELMAN, G., 2007, ICESat full waveform altimetry compared to airborne laser altimetry over The Netherlands. In *ISPRS Workshop on Laser Scanning 2007 and SilviLaser 2007*, 12–14 September 2007, Espoo, Finland, pp. 108–113.

DUONG, H., PFEIFER, N. and LINDENBERGH, R., 2006, Full waveform analysis: ICESat laser data for land cover classification. In *ISPRS Commission VII Mid-term Symposium Remote Sensing: From Pixels to Processes*, 8–11 May 2006, Enschede, The Netherlands, pp. 30–35.

FABRICE, P., BENOÎT, L. and FRÉDÉRIQUE, R., 2003, Use of the Topex–Poseidon dual-frequency radar altimeter over land surfaces. *Remote Sensing of Environment*, **87**, pp. 136–147.

FARRELL, S.L., LAXON, S.W., MCADOO, D.C., YI, D. and ZWALLY, H.J., 2009, Five years of Arctic sea ice freeboard measurements from the Ice, Cloud, and land Elevation Satellite. *Journal of Geophysical Research*, **114**, C04008, doi:10.1029/2008JC005074.

FORSBERG, R. and SKOURUP, H., 2005, Arctic Ocean gravity, geoid and sea ice freeboard heights from ICESat and GRACE. *Geophysical Research Letters*, **32**, L21502, doi:10.1029/2005GL023711.

FRICKER, H.A. and PADMAN, L., 2006, Ice shelf grounding zone structure from ICESat laser altimetry. *Geophysical Research Letters*, **33**, L15502, doi:10.1029/2006GL026907.

FRICKER, H.A., SCAMBOS, T., BINDSCAHADLER, R. and PADMAN, L., 2007, An active subglacial water system in West Antarctica mapped from space. *Science*, **315**, pp. 1544–1548.

Gong, P., Biging, G.S., Lee, S.M., Mei, X., Sheng, Y., Pu, R., Xu, B. and Schwarz, K.-P., 1999, Photo-ecometrics for forest inventory. *Geographic Information Sciences*, **5**, pp. 9–14.

Gong, P., Biging, G.S. and Standiford, R., 2000, The potential of digital surface model for hardwood rangeland monitoring. *Journal of Range Management*, **53**, pp. 622–626.

Gong, P., Li, Z., Huang, H.B., Sun, G.Q. and Wang, L., 2011, ICEsat GLAS data for urban environment monitoring. *IEEE Transactions on Geosciences and Remote Sensing*, **49**, pp. 1158–1172, doi: 10.1109/TGRS.2010.2070514.

Gong, P., Pu, R. and Yu, B., 2001, Conifer species recognition: effects of data transformation and band width. *International Journal of Remote Sensing*, **22**, pp. 3471–3481.

Gong, P., Sheng, Y. and Biging, G.S., 2002, 3D model-based tree measurement from high resolution aerial imagery. *Photogrammetric Engineering & Remote Sensing*, **68**, pp. 1203–1212.

Gwenzi, D., 2008, Spaceborne LiDAR canopy height estimation for aboveground forest biomass assessment in the Cool Montane area of north east China. Masters thesis, International Institute for Geo-information Science and Earth Observation, The Netherlands.

Harding, D.J. and Carabajal, C.C., 2005, ICESat waveform measurements of within-footprint topographic relief and vegetation vertical structure. *Geophysical Research Letters*, **32**, L21S10, doi:10.1029/2005GL023471.

Harding, D.J., Lefsky, M.A., Parker, G.G. and Blair, J.B., 2001, Laser altimeter canopy height profiles – methods and validation for closed canopy, broadleaf forests. *Remote Sensing of Environment*, **76**, pp. 283–297.

Hart, W.D., Palm, S.P. and Hlavka, D.L., 2005, LiDAR global cloud and aerosol layer distribution statistics from GLAS observation. Available online at: http://ams.confex.com/ams/pdfpapers/86261.pdf (accessed 30 July 2010).

Hlavka, D.L., Palm, S.P., Hart, W.D., Spinhirne, J.D., McGill, M.J. and Welton, E.J., 2005, Aerosol and cloud optical depth from GLAS: results and verification for an October 2003 California fire smoke case. *Geophysical Research Letters*, **32**, L22S07, doi:10.1029/2005 GL023413.

Hofton, M.A., Minster, J.B. and Blair, J.B., 2000, Decomposition of laser altimeter waveforms. *IEEE Transactions on Geoscience and Remote Sensing*, **38**, pp. 1989–1996.

Huang, H., Gong, P., Cheng, X., Clinton, N. and Li, Z., 2009, Improving measurement of forest structural parameters by co-registering of high resolution aerial imagery and low density LiDAR data. *Sensors*, **9**, pp. 1541–1558.

ICESAT/GLAS Science Computing Team, 2008, Visualization software user's guide, Version 200807.0, July 2008. Available online at: http://nsidc.org/data/icesat/tools.html (accessed 12 May 2010).

IPCC, 2007, Fourth assessment review. Available online at: http://www.ipcc.ch/publications_and_data/publications_ipcc_fourth_assessment_report_synthesis_report.htm (accessed 17 November 2010).

Ivins, E.R., 2009, Ice sheet stability and sea level. *Science*, **324**, pp. 888–889.

Kääb, A., 2008, Glacier volume changes using ASTER satellite stereo and ICESat GLAS laser altimetry. A test study on Edgeøya, Eastern Svalbard. *IEEE Transactions on Geoscience and Remote Sensing*, **46**, pp. 2823–2830.

Kichak, R., 2003, Independent GLAS Anomaly Review Board executive summary. Available online at: http://icesat.gsfc.nasa.gov/docs/IGARB.pdf (accessed 1 September 2010).

Kim, J.W., Lu, Z., Lee, H., Shum, C.K., Swarzenskic, C.M., Doyle, T.W. and Baek, S.H., 2009, Integrated analysis of PALSAR/Radarsat-1 InSAR and ENVISAT altimeter data for mapping of absolute water level changes in Louisiana wetlands. *Remote Sensing of Environment*, **113**, pp. 2356–2365.

Klokočník, J., Kostelecký, J. and Wagner, C.A., 2008, Improvement in the radial accuracy of altimeter-satellite orbits due to the geopotential. *Earth-Science Reviews*, **91**, pp. 106–120.

KURTZ, N.T., MARKUS, T., CAVALIERI, D.J., KRABILL,W., SONNTAG, J.G. and MILLER, J., 2008, Comparison of ICESat data with airborne laser altimeter measurements over Arctic sea ice. *IEEE Transactions on Geoscience and Remote Sensing*, **46**, pp. 1913–1924.

KWOK, R. and CUNNINGHAM, G.F., 2008, ICESat over Arctic sea ice: estimation of snow depth and ice thickness. *Journal of Geophysical Research*, **113**, C08010, doi:10.1029/2008JC004753.

KWOK, R., CUNNINGHAM, G.F., ZWALLY, H.J. and YI, D., 2006, ICESat over Arctic sea ice: interpretation of altimetric and reflectivity profiles. *Journal of Geophysical Research*, **111**, C06006, doi:10.1029/2005JC003175.

KWOK, R., CUNNINGHAM, G.F., ZWALLY, H.J. and YI, D., 2007, Ice, Cloud, and land Elevation Satellite (ICESat) over Arctic sea ice: retrieval of freeboard. *Journal of Geophysical Research*, **112**, C12013, doi:10.1029/2006JC003978.

KWOK, R., ZWALLY, H.J. and YI, D., 2004, ICESat observations of Arctic sea ice: a first look. *Geophysical Research Letters*, **31**, L16401, doi:10.1029/2004GL020309.

LAURENCE, N.C., SEYMOUR, W.L., ANDREW, L.R., WILLIAM, B.K. and DAVID, C.M., 2009, Comparison of Envisat radar and airborne laser altimeter measurements over Arctic sea ice. *Remote Sensing of Environment*, **113**, pp. 563–570.

LAXON, S.W., PEACOCK, N. and SMITH, D., 2003, High interannual variability of sea ice thickness in the Arctic region. *Nature*, **425**, pp. 947–949.

LEFSKY, M.A., 2010, A global forest canopy height map from the Moderate Resolution Imaging Spectroradiometer and the Geoscience Laser Altimeter System. *Geophysical Research Letters*, **37**, L15401, doi:10.1029/2010GL043622.

LEFSKY, M.A., COHEN, W.B., ACKER, S.A., PARKER, G.G., SPIES, T.A. and HARDING, D., 1999a, LiDAR remote sensing of the canopy structure and biophysical properties of Douglas-fir western hemlock forests. *Remote Sensing of Environment*, **70**, pp. 339–361.

LEFSKY, M.A., HARDING, D., COHEN, W.B., PARKER, G. and SHUGART, H.H., 1999b, Surface LiDAR remote sensing of basal area and biomass in deciduous forests of Eastern Maryland, USA. *Remote Sensing of Environment*, **67**, pp. 83–98.

LEFSKY, M.A., HARDING, D.J., KELLER, M., COHEN, W.B., CARABAJAL, C.C., ESPIRITO-SANTO, F.D., HUNTER, M.O. and DE OLIVEIRA, R., 2005, Estimates of forest canopy height and aboveground biomass using ICESat. *Geophysical Research Letters*, **32**, L22S02, doi:10.1029/2005GL023971.

LEFSKY, M.A., KELLER, M., PANG, Y., DE CAMARGO, P.B. and HUNTER, M.O., 2007, Revised method for forest canopy height estimation from Geoscience Laser Altimeter System waveforms. *Journal of Applied Remote Sensing*, **1**, 013537.

LEGRESY, B., PAPA, F., REMY, F., VINAY, G., BOSCH, M.V.D. and ZANIFE, O.Z., 2005, ENVISAT radar altimeter measurements over continental surfaces and ice caps using the ICE-2 retracking algorithm. *Remote Sensing of Environment*, **95**, pp. 150–163.

LINDSAY, R.W. and ZHANG, J., 2005, The thinning of Arctic sea ice 1988–2003: have we passed a tipping point? *Journal of Climate*, **18**, pp. 4879–4894.

MAHESH, A., GREY, M.A., PALM, S.P., HART, W.D. and SPINHIRNE, J.D., 2004, Passive and active detection of clouds: comparisons between MODIS and GLAS observations. *Geophysical Research Letters*, **31**, L04108, doi:10.1029/2003GL018859.

MCGILL, M.J., HLAVKA, D.L., HART, W.D., PALM, S.P., WINTER, D.M., VAUGHAN, M.A., POWELL, K.A. and SPINHIRNE, J.D., 2005, The Cloud Physics LiDAR and application to spaceborne LiDAR validation. Available online at: http://ams.confex.com/ams/pdfpapers/85607.pdf (accessed 19 June 2010).

MCINTYRE, N., 1991, Mapping ice sheets with the altimeter. *International Journal of Remote Sensing*, **12**, pp. 1775–1793.

MENG, X.L., WANG, L. and CURRIT, N., 2009, Morphology-based building detection from airborne LiDAR data. *Photogrammetric Engineering and Remote Sensing*, **75**, pp. 437–442.

MOLIJN, R.A., LINDENBERGH, R.C. and GUNTER, B.C., 2011, ICESat laser full waveform analysis for the classification of land cover types over the cryosphere. *International Journal of Remote Sensing*.

NEUENSCHWANDER, A.L., URBAN, T.J., GUTIERREZ, R. and SCHUTZ, B.E., 2008, Characterization of ICESat/GLAS waveforms over terrestrial ecosystems: implications for vegetation mapping. *Journal of Geophysical Research*, **113**, G02S03, doi:10.1029/2007JG000557.

NEUMANN, M., FERRO-FAMIL, L. and REIGBER, A., 2010, Estimation of forest structure, ground, and canopy layer characteristics from multibaseline polarimetric interferometric SAR data. *IEEE Transactions on Geoscience and Remote Sensing*, **48**, pp. 1086–1104.

PALM, S., HART, W., HLAVKA, D., WELTON, E.J., MAHESH, A. and SPINHIRNE, J., 2002, Geosciences Laser Altimeter System (GLAS) atmospheric data products, algorithm theoretical basis document, Version 4.2 (Greenbelt, MD: NASA Goddard Space Flight Center).

PANG, Y., LEFSKY, M., ANDERSEN, H.E., MILLER, M.E. and SHERRILL, K., 2008, Validation of the ICESat vegetation product using crown-area-weighted mean height derived using crown delineation with discrete return LiDAR data. *Canadian Journal of Remote Sensing*, **34**, pp. S471–S484.

PAPA, F., LEGRÉSY, B. and RÉMY, F., 2003, Use of the Topex–Poseidon dual-frequency radar altimeter over land surfaces. *Remote Sensing of Environment*, **87**, pp. 136–147.

PATENAUDE, G., MILNE, R. and DAWSON, T.P., 2005, Synthesis of remote sensing approaches for forest carbon estimation: reporting to the Kyoto protocol. *Environmental Science & Policy*, **8**, pp. 161–178.

REES, W.G., 2006, *Remote Sensing of Snow and Ice*, pp. 1–22 (London: CRC Press).

RIGNOT, E.J. and KANAGARATNAM, P., 2006, Changes in the velocity structure of the Greenland ice sheet. *Science*, **311**, pp. 986–990.

ROSETTE, J.A.B., NORTH, P.R.J. and SUAREZ, J.C., 2008, Vegetation height estimates for a mixed temperate forest using satellite laser altimetry. *International Journal of Remote Sensing*, **29**, pp. 1475–1493.

ROTHROCK, D.A., YU, Y. and MAYKUT, G.A., 1999, Thinning of the Arctic sea-ice cover. *Geophysical Research Letters*, **26**, pp. 3469–3472.

SAUBER, J.M., MOLNIA, J.B., CARABAJAL, C., LUTHCKE, S. and MUSKETT, R., 2005, Ice elevations and surface change on the Malaspina Glacier, Alaska. *Geophysical Research Letters*, **32**, L23S01, doi:10.1029/2005GL023943.

SAUER, S., FERRO-FAMIL, L., REIGBER, A. and POTTIER, E., 2009, Polarimetric dual-baseline INSAR building height extraction at L-Band. *IEEE Geoscience and Remote Sensing Letters*, **6**, pp. 408–412.

SCHUTZ, B.E., 1998, Spaceborne laser altimetry: 2001 and beyond. In *Proceedings of WEBENER-98*, Norwegian Mapping Authority, Honefoss, Norway.

SCHUTZ, B.E, 2002, Laser footprint location (geolocation) and surface profiles, algorithom theoretical basis document, Version 3.0 (Greenbelt, MD: NASA Goddard Flight Center).

SCHUTZ, B.E., ZWALLY, H.J., SHUMAN, C.A, HANCOCK, D. and DIMARZIO, J.P., 2005, Overview of the ICESat Mission. *Geophysical Research Letters*, **32**, L21S01, doi:10.1029/2005GL024009.

SHIOBARA, M., YABUKI, M., SPINHIRNE, J.D., WELTON, E.J., CAMPBELL, J.R., BERKOFF, T.A., NEUBER, R., OSADA, K. and HASHIDA, G., 2004, Cloud and Aerosol Observations by Micro-Pulse LiDARs at Arctic and Antarctic Sites During ICESat/GLAS Overpass Measurements. In *AGU Fall Meeting*, 13–17 December 2004, San Francisco, USA.

SHUMAN, C.A., ZWALLY, H.J., SCHUTZ, B.E., BRENNER, A.C., DIMARZIO, J.P., SUCHDEO, V.P. and FRICKER, H.A., 2006, ICESat Antarctic elevation data: preliminary precision and accuracy assessment. *Geophysical Research Letters*, **33**, L07501, doi:10.1029/2005GL025227.

SIMARD, M., RIVERA-MONROY, V.H., MANCERA-PINEDA, J.E., CASTAÑEDA-MOYA, E. and TWILLEY, R.R., 2008, A systematic method for 3D mapping of mangrove forests based on Shuttle Radar Topography Mission elevation data, ICEsat–GLAS waveforms and field data application to Cinaga Grande de Santa Marta, Colombia. *Remote Sensing of Environment*, **112**, pp. 2131–2144.

SIROTA, J.M., BAE, S., MILLAR, P., MOSTOFI, D., WEBB, C., SCHUTZ, B. and LUTHCKE, S., 2005, The transmitter pointing determination in the Geoscience Laser Altimeter System. *Geophysical Research Letters*, **32**, L22S11, doi:10.1029/2005GL024005.

SLOBBE, D.C., LINDENBERGH, R.C. and DITMAR, P., 2008, Estimation of volume change rates of Greenland's ice sheet from ICESat data using overlapping footprints. *Remote Sensing of Environment*, **112**, pp. 4204–4213.

SMITH, B.E., BENTLEY, C.R. and RAYMOND, C.F., 2005, Recent elevation changes on the ice streams and ridges of the Ross Embayment from ICESat crossovers. *Geophysical Research Letters*, **32**, L21S09, doi:10.1029/2005GL024365.

SNEED, W.A., HOOK, R.L. and HAMILTON, G.S., 2008, Thinning of the south dome of Barnes ice cap, Arctic Canada, over the past two decades. *Geology*, **36**, pp. 71–74.

SPINHIRNE, J.D., PALM, S.P. and HART, W.D., 2005a, Antarctica cloud cover for October 2003 from GLAS satellite LiDAR profiling. *Geophysical Research Letters*, **32**, L22S05, doi:10.1029/ 2005GL023782.

SPINHIRNE, J.D., PALM, S.P., HART, W.D., HLAVKA, D.L. and WELTON, E.J., 2005b, Cloud and aerosol measurements from GLAS: overview and initial results. *Geophysical Research Letters*, **32**, L22S03, doi:10.1029/2005GL023507.

SPINHIRNE, J.D., PALM, S.P., HLAVKA, D.L., HART, W.D., MAHESH, A. and WELTON, E.J., 2004, Aerosol and cloud measurements at 532 and 1064 nm by the GLAS polar orbiting LiDAR instrument. In *Proceedings of Geoscience and Remote Sensing Symposium, IGARSS '04*, pp. 3956–3959 (IEEE International).

STEWART, C. and HESSAMI, M.-A., 2005, A study of methods of carbon dioxide capture and sequestration-the sustainability of a photosysthetic bioreactor approach. *Energy Conversion and Management*, **46**, pp. 403–420.

SUN, G., RANSON, K.J., KIMES, D.S., BLAIR, J.B. and KOVACS, K., 2008, Forest vertical structure from GLAS: an evaluation using LVIS and SRTM data. *Remote Sensing of Environment*, **112**, pp. 107–117.

TOKMAKIAN, R.T., CHALLENOR, P.G., GUYMER, T.H. and SROKOSZ, M.A., 1994, The U.K. EODC ERS-1 altimeter oceans processing scheme. *International Journal of Remote Sensing*, **15**, pp. 939–962.

URBAN, T.J., SCHUTZ, B.E. and NEUENSCHWANDER, A.L., 2008, A survey of ICESat coastal altimetry applications: continental coast, open ocean island, and inland river. *Terrestrial Atmospheric and Oceanic Sciences*, **19**, pp. 1–19.

WEISHAMPEL, J.F., BLAIR, J.B., KNOX, R.G., DUBAYAH, R. and CLARK, D.B., 2000, Volumetric LiDAR return patterns from an old-growth tropical rainforest canopy. *International Journal of Remote Sensing*, **21**, pp. 409–415.

WINGHAM, D.J., RIDOUT, A.J., SCHARROO, R., ARTHERN, R.J. and SHUM, C.K., 1998, Antarctic elevation change from 1992 to 1996. *Science*, **282**, pp. 456–458.

YANG, Y., MARSHAK, A., CHIU, J.C., WISCOMBE, W.J., PALM, S.P., DAVIS, A.B., SPANGENBERG, D.A., NGUYEN, L., SPINHIRNE, J.D. and MINNIS, P.I., 2008, Retrievals of thick cloud optical depth from the Geoscience Laser Altimeter System (GLAS) by calibration of solar background signal. *Journal of Atmospheric Sciences*, **65**, pp. 3513–3527.

YI, D., ZWALLY, H.J. and SUN, X., 2005, ICESat measurement of Greenland ice sheet surface slope and roughness. *Annals of Glaciology*, **42**, pp. 83–89.

Zwally, H.J., 2010, ICESat Cryosphere Sciences Branch Code 614.1. Available online at: http://icesat.gsfc.nasa.gov/icesat/ (accessed 11 May 2010).

Zwally, H.J., Schutz, B., Abdalati, W., Abshire, J., Bentley, C., Brenner, A., Bufton, J., Dezio, J., Hancock, D., Harding, D., Herring, T., Minster, B., Quinn, K., Palm, S., Spinhirne, J. and Thomas, R., 2002, ICESat's laser measurements of polar ice, atmosphere, ocean, and land. *Journal of Geodynamics*, **34**, pp. 405–445.

Zwally, H.J., Yi, D., Kwok, R. and Zhao, Y., 2008, ICESat measurements of sea ice freeboard and estimates of sea ice thickness in the Weddell Sea. *Journal of Geophysical Research*, **113**, C02S15, doi:10.1029/2007JC004284.